29.0 IDENTIFICATION OF DEFORMATION MECHANISMS IN THERMALLY STABLE CAST AL-CU ALLOYS *VIA* NEUTRON DIFFRACTION

Brian Milligan
Faculty: Amy Clarke (Mines)
Co-Advisor: Amit Shyam (ORNL)
Industrial Mentor: John Carpenter (LANL)

This project initiated in Fall 2017 and is supported by CANFSA and the GO! program at Oak Ridge National Lab. The research performed during this project will serve as the basis for a Ph.D. thesis program for Brian Milligan.

29.1 Project Overview and Industrial Relevance

Cast Al-Cu alloys have long been popular in applications that require complex shapes, low density, and high strength. One such application is cylinder heads for internal combustion engines. However, as temperatures in commercial engines increase, the precipitates in these alloys begin to coarsen and transform during service. This leads to a loss of strength, due to larger precipitate spacings and a change in deformation mechanisms [29.1].

Due to the anisotropy that arises during strain hardening in these alloys, an approach that takes orientation and phase into account is useful in studying their mechanical properties. These insights may be used to inform future efforts in alloy development and heat treating to improve properties such as ductility and fatigue performance.

In order to study the strain hardening behavior of cast Al-Cu alloys as a function of orientation and phase, *in situ* time-of-flight neutron diffraction experiments were completed at the VULCAN beamline at the Spallation Neutron Source at Oak Ridge National Laboratory. This technique allows for the measurement of stresses in multiple phases during a mechanical test as a function of orientation. The alloy of primary interest in the present work is cast Al-Cu alloy 206 (composition in **Table 29.1**).

29.2 Previous Work

29.2.1 Literature Review

Al-Cu precipitation has been studied in detail and generally follows the following transformation pathway: supersaturated solid solution → plate-shaped, single atomic layer Guinier-Preston (GP) I zones → plate-shaped, 2-4 layer GPII/θ'' precipitates → thick, plate shaped θ' precipitates → approximately spherical or rod-shaped θ equilibrium precipitates [29.1]. These precipitates are displayed and labeled in TEM micrographs in **Figure 29.1.** This range of precipitate sizes, morphologies, and structures leads to a large difference in mechanical properties with even small difference in aging treatment of Al-Cu alloys. With modern computational tools and experimentation, models to describe these quantities are being continually refined. Of particular interest is the work of da Costa Teixiera *et al.*, who have improved the accuracy of yielding and strain hardening predictions for Al-Cu alloys by not using the common assumption of spherical precipitates [29.2,3].

The studies mentioned above have mostly looked at mechanical behavior of precipitate strengthened alloys in a bulk, continuum manner. Recently, however, there has been significant interest in the precipitate-dislocation interactions at an individual precipitate scale, as these interactions are important in determining strain hardening behavior. Two such studies come from Krasnikov *et al.* and Kaira *et al.*¸ whom have studied the shearing behavior of θ' precipitates using dislocation dynamics and atomistic simulations and 4-D X-ray imaging methods, respectively [29.4,5]. These studies corroborate with the bulk modeling by da Costa Teixeira *et al.*, all three of which predict that precipitates will be bypassed by dislocations at the yield of the bulk material, but will later be sheared by dislocations in a process referred to as delayed shearing.

An additional area of interest to this work is the concept of load transfer, which occurs in a two-phase aggregate when one phase is significantly stronger than the other. When the weaker phase yields and begins *plastic* deformation, the stronger phase must undergo a similar amount of *elastic* deformation to prevent the formation of voids [29.6]. These large elastic strains translate to large stresses in the precipitates, which contribute to the strain

hardening behavior of the aggregate. Load transfer can occur in an anisotropic manner if the precipitates are high aspect ratio [29.7]. The high aspect ratio precipitates can accommodate some shear strain by rotation, which reduces the magnitude of load transfer, but it is a strong function of orientation of the precipitate, as shown in **Figure 29.2**.

29.2.2 Identification of Deformation Mechanisms and Modeling of Load Transfer at Room Temperature

Specimens were prepared with multiple aging treatments (**Table 29.2**) to study the strain hardening behavior as a function of orientation, phase and precipitate structure. The precipitate structures of each of these conditions is shown in **Figure 29.1**. The peak aged condition contains GPI zones and θ'' precipitates, the 200°C overaged condition contains θ' precipitates, and the 300°C overaged condition contains θ' and θ precipitates.

The results from the neutron diffraction experiments are shown in **Figure 29.3**. On the Y-axis is applied stress and the X-axis is lattice strain. Lattice strain represents a difference in lattice planar spacing, which is directly proportional to stress within a family of grain orientations or precipitate orientations. Load transfer can be observed when the behavior of the two phases significantly deviate from one another, as shown in **Figure 29.3 (b) and (c)**. Two different precipitate-dislocation interactions were identified for the three precipitate structures using this load transfer observation. The small amount of load transfer in the peak aged condition indicates precipitate shearing [29.8]. In the 200 and 300°C overaged conditions, there was significant load transfer, indicating bypass of precipitates by dislocations *via* either Orowan looping or cross-slip. The 200°C overaged condition also displayed highly anisotropic load transfer behavior, which can be observed by the highly variable strain hardening rates in the different matrix crystallographic orientations. The 300°C overaged condition displayed unpredictable behavior and a decrease in lattice strain at the end of the experiment, indicating fracture of the precipitates [29.9].

The highly anisotropic load transfer behavior was concluded to be caused by rotation of the precipitates, as discussed by Hosford *et al* [29.7], and is displayed in **Figure 29.1**, where shear strains in the matrix surrounding the precipitate can be accommodated *via* rotation in (c). This phenomenon was modeled using a mechanics approach, using the following steps. First, two sources of stress were assumed in the precipitate: 1. Applied stress from the load frame (σ_{app}^{hkl}) and stress transferred from the matrix ($\sigma_{transfer}^{hkl,p}$). These stresses were changed to elastic strains using the crystallographic orientation-specific elastic moduli for the precipitate (E_p^{hkl}) i.e.

$$\epsilon_{lattice}^{hkl,p} = \frac{\sigma_{total}^{hkl}}{E_p^{hkl}} = \frac{\sigma_{app}}{E_p^{hkl}} + \frac{\sigma_{transfer}^{hkl,p}}{E_p^{hkl}} \tag{29.1}$$

where σ_{app} is applied stress and $\epsilon_{lattice}^{hkl,p}$ is the lattice strain in the precipitate, directly comparable to the same value measured using neutron diffraction. The transferred stress was measured using a transfer strain term, i.e.

$$\epsilon_{tranfer}^{hkl,p} = \frac{\sigma_{transfer}^{hkl,p}}{E_p^{hkl}} \tag{29.2}$$

and $\epsilon_{tranfer}^{hkl,p}$ was calculated using two assumptions: the precipitates did not yield, and perfect load transfer (after accounting for rotation). These assumptions mean that the transfer strain is equal to the total strain in the matrix (assumed to be uniaxial in the tensile direction), minus any shear strains present (relative to the major and minor axes of the precipitate). For more information, see B. Milligan's Spring 2020 CANFSA report. A paper on this topic has also been submitted to Acta Materialia.

The lattice strains in the matrix were then calculated using the assumption of load sharing between the two phases, i.e.

$$\sigma_{app} = \epsilon_{lattice}^{hkl,p} E_p^{hkl} V_f^p + \epsilon_{lattice}^{hkl,m} E_m^{hkl} (1 - V_f^p) \tag{29.3}$$

where V_f^p is the precipitate volume fraction (measured using TEM). This equation was solved $\epsilon_{lattice}^{hkl,m}$, translated to $\sigma_{lattice}^{hkl,m}$ using the elastic modulus, then used to build strain hardening curves for the matrix, and is compared against the measured strain hardening rates in **Figure 29.4.**

29.3 Recent Progress

29.3.1 Identification of Deformation Mechanisms at Elevated Temperature in Alloy RR350

Alloy RR350 is an Al-Cu-Ni alloy with Mn and Zr alloying additions that segregate to the θ′ interfaces and prevent the transformation of precipitates up to a temperature of 350°C [29.8], as shown in **Figure 29.5**. The composition of the alloy is shown in **Table 29.1,** and the aging treatments are shown in **Table 29.2**. The resistance of the alloy to coarsening and transformation of the θ′ precipitates make it a perfect candidate for the study of precipitate-dislocation interactions in Al-Cu alloys at elevated temperatures. Here, we perform the same neutron diffraction experiments as were done on alloy 206 at temperatures ranging from room temperature (RT) to 350°C.

Lattice strain evolution curves are shown in **Figure 29.6**. The primary conclusion that can be drawn from this figure is that, in each of the aging conditions, the precipitate lattice strains reach a maximum value before decreasing. This observation is indicative of precipitate bypass via Orowan looping or cross-slip in the beginning of the test, then another deformation mechanism taking control later in the experiment. Evidence for Orowan looping can be seen in the post-mortem TEM, as shown in **Figure 29.7**. Note in both the room temperature experiment and the 300°C experiment, dislocations can be observed on the interfaces of the in-plane precipitates, with highly disorganized dislocations at room temperature and highly organized dislocations at 300°C. This organization is taken as evidence of dynamic recovery.

There are two primary mechanisms by which the lattice strains in the precipitate may be decreased: delayed precipitate shearing [29.2] and climb of Orowan loops [29.9]. The first occurs when extensive load transfer happens during the initial plastic deformation of the alloy, leading to a stress in the precipitate high enough to shear it at higher plastic strains. This shearing process involves the collapse of Orowan loops that sit on the slip plane that was sheared. The second mechanism occurs at high temperature and low strain rate (which, in these experiments was controlled at 10^{-5} s^{-1}), and involves Orowan loops climbing until they no longer surround a precipitate, leading to their collapse. Both mechanisms reduce the dislocation density around the precipitate, and therefore reduce the local stress.

Additional evidence of the reduction in Orowan loop density around the precipitates (and therefore evidence for one of these two precipitate-dislocation interactions) is shown by the peak width evolution curves (**Figure 29.8**). An increase in the peak width is caused by strain gradients, and is usually indicative of increasing dislocation density, and therefore the increase in peak width in the matrix at lower temperatures is expected. The strain gradients due to dislocations can also penetrate coherent interfaces, such as the one on the broad face of θ′ precipitates [29.10], and therefore the increase in peak width at lower strains in all the experiments is taken as evidence for Orowan looping. By extension, the decrease in peak width of the precipitate at higher strain is taken as alternative deformation mechanisms decreasing the Orowan loop density. This observation consistently happens at similar strain levels to the decrease in precipitate lattice strain observed earlier.

29.4 Plans for Next Reporting Period

The room-temperature analysis of alloy 206 is complete and a journal article has been submitted to Acta Materialia. Analysis of elevated temperature response of alloy RR350 is underway. Future work includes:
- Continued analysis of elevated temperature results on alloy RR350;
- Application of an existing model or development of a new model describing the elevated temperature shear strength of the θ′ precipitates in alloy RR350;
- Writing of a journal article on the elevated temperature results;
- Starting analysis on the creep behavior of several alloys at different temperatures using neutron diffraction.

29.5 References

[29.1] S. Roy, L.F. Allard, A. Rodriguez, T.R. Watkins, A. Shyam, Comparative Evaluation of Cast Aluminum Alloys for Automotive Cylinder Heads: Part I—Microstructure Evolution, Metall. Mater. Trans. A. 48 (2017) 2529–2542. https://doi.org/10.1007/s11661-017-3985-1.

[29.2] J. da Costa Teixeira, L. Bourgeois, C.W. Sinclair, C.R. Hutchinson, The effect of shear-resistant, plate-shaped precipitates on the work hardening of Al alloys: Towards a prediction of the strength–elongation correlation, Acta Mater. 57 (2009) 6075–6089. https://doi.org/10.1016/j.actamat.2009.08.034.

[29.3] J. da Costa Teixeira, D.G. Cram, L. Bourgeois, T.J. Bastow, A.J. Hill, C.R. Hutchinson, On the strengthening response of aluminum alloys containing shear-resistant plate-shaped precipitates, Acta Mater. 56 (2008) 6109–6122. https://doi.org/10.1016/j.actamat.2008.08.023.

[29.4] V.S. Krasnikov, A.E. Mayer, Dislocation dynamics in aluminum containing θ' phase: Atomistic simulation and continuum modeling, Int. J. Plast. 119 (2019) 21–42. https://doi.org/10.1016/j.ijplas.2019.02.010.

[29.5] C.S. Kaira, T.J. Stannard, V. De Andrade, F. De Carlo, N. Chawla, Exploring novel deformation mechanisms in aluminum–copper alloys using in situ 4D nanomechanical testing, Acta Mater. 176 (2019) 242–249. https://doi.org/10.1016/j.actamat.2019.07.016.

[29.6] S. Ma, V. Seetharaman, B.S. Majumdar, CRSS of γ/γ′ phases from in situ neutron diffraction of a directionally solidified superalloy tension tested at 900°C, Acta Mater. 56 (2008) 4102–4113. https://doi.org/10.1016/j.actamat.2008.04.057.

[29.7] W.F. Hosford, R.H. Zeisloft, The anisotropy of age-hardened Al-4 pct Cu single crystals during plane-strain compression, Metall. Mater. Trans. B. 3 (1972) 113–121. https://doi.org/10.1007/BF02680590.

[29.8] A. Shyam, S. Roy, D. Shin, J.D. Poplawsky, L.F. Allard, Y. Yamamoto, J.R. Morris, B. Mazumder, J.C. Idrobo, A. Rodriguez, T.R. Watkins, J.A. Haynes, Elevated temperature microstructural stability in cast AlCuMnZr alloys through solute segregation, Mater. Sci. Eng. A. 765 (2019) 138279. https://doi.org/10.1016/j.msea.2019.138279.

[29.9] R. Monzen, H. Mizutani, Climb of Orowan loops in an overaged Al–Li alloy, Mater. Sci. Eng. A. 231 (1997) 105–110. https://doi.org/10.1016/S0921-5093(97)00066-X.

[29.10] X. Wang, P. Schiavone, A screw dislocation interacting with a bimaterial interface incorporating surface strain gradient elasticity, Eur. J. Mech. - ASolids. 53 (2015) 254–258. https://doi.org/10.1016/j.euromechsol.2015.05.010.

29.6   Figures and Tables

Table 29.1: Composition of alloys 206 and RR350, in weight percent.

Alloy	Cu	Mn	Zr	Si	Mg	Zn	Fe	Ni	Co	Ti	Sb
206	4.5	0.23		0.12	0.30		0.14			0.02	
RR350	4.8	0.19	0.17	0.05		0.01	0.09	1.2	0.26	0.21	0.17

Table 29.2: Description of the heat treatments applied prior to neutron diffraction analysis. OA stands for overage.

Alloy	Condition	Solutionize	Quench	Peak Age	Overage
206	Natural Age	530°C for 5h	80-90°C in water	None	None
	200°C OA			190°C for 5h	200°C for 200hr
	300°C OA				300°C for 200hr
RR350	As-Aged	535°C for 5h	80-90°C for >1h	220°C for 4h	None
	100°C				100°C for 200hr
	200°C				200°C for 200hr
	300°C				300°C for 200hr
	350°C				350°C for 200hr
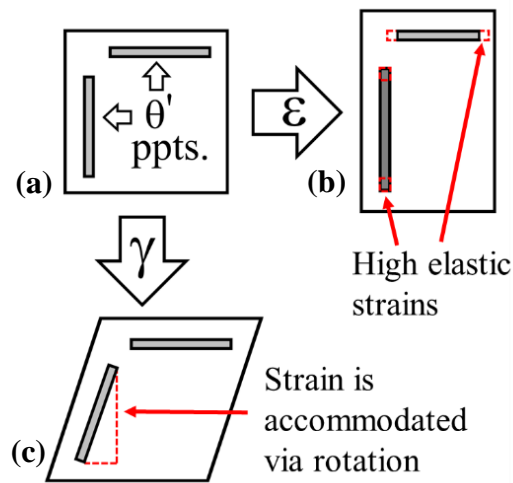
Figure 29.1: Schematic of load transfer and strain accommodation *via* rotation. (a) Precipitates with little elastic strain prior to the tension test. (b) Tensile strain is applied vertically, and the matrix deforms plastically, while the precipitates deform elastically. (c) Shear strain is applied, and the matrix deforms plastically while the precipitates rotate to accommodate the strain.
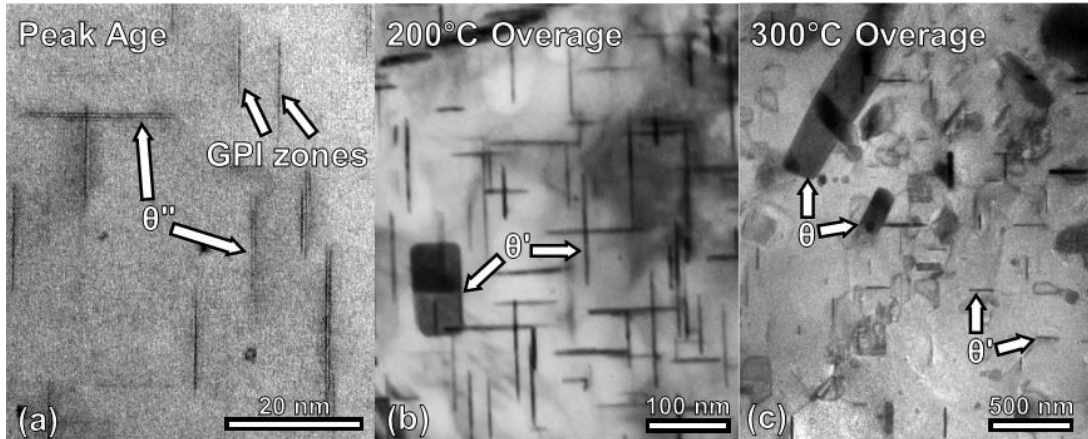
Figure 29.2: Bright field STEM (a,c) and TEM (b) images of the precipitate structures of Al-Cu alloy 206 in three aging conditions (**Table 2**). All zone axes are [001]$_\alpha$. Note the differences in scale between the images.
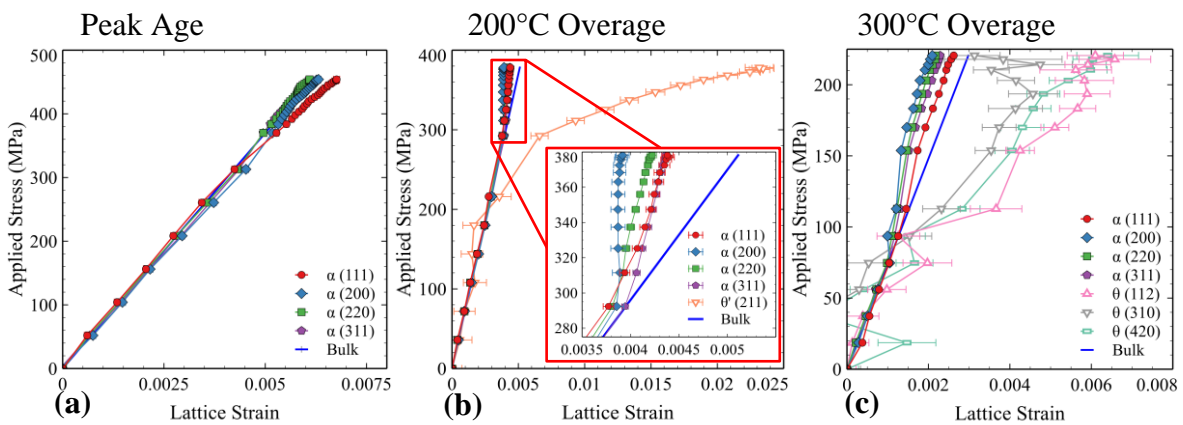

Figure 29.3: Applied stress versus lattice strain plots showing load transfer in the 200 and 300°C overaged conditions (b,c), as well as anisotropic strain hardening in the 200°C overaged condition (inset in (b)).
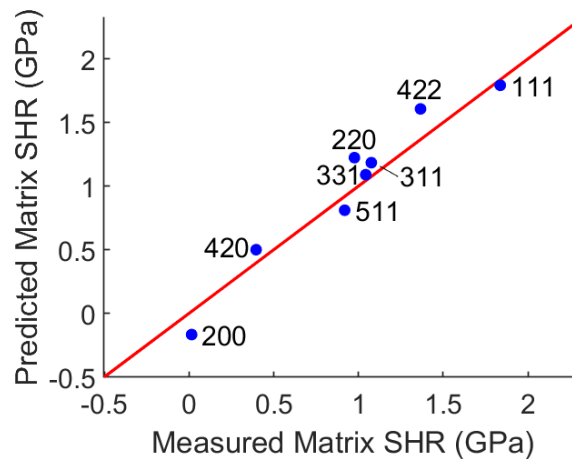

Figure 29.4: Predicted strain hardening rates in the matrix from **Equation 29.3**. Note the close prediction of both the trend in the anisotropic strain hardening, as well as the actual strain hardening rates. A Y=X line has been included to show theoretically perfect predictions.
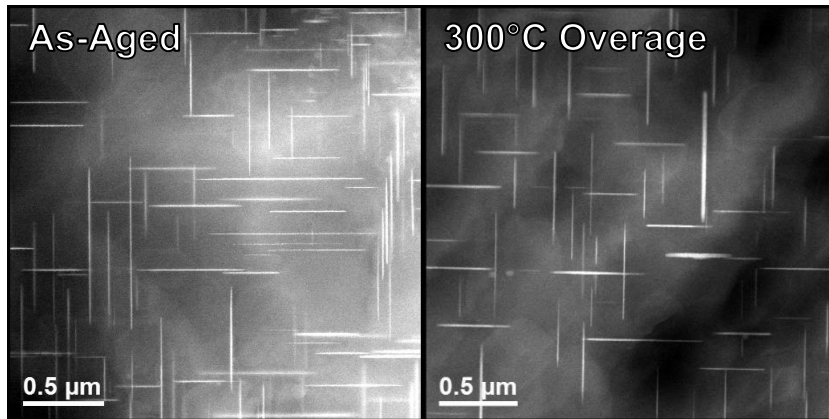
29.6

Figure 29.5: STEM-HAADF images of the (a) as-aged RR350 and (b) 300°C preconditioned RR350. Note the prevalence of θ′ in both images, with little change in size or distribution. Zone axis in both images is {001}$_\alpha$. Images courtesy of Lawrence Allard (ORNL).
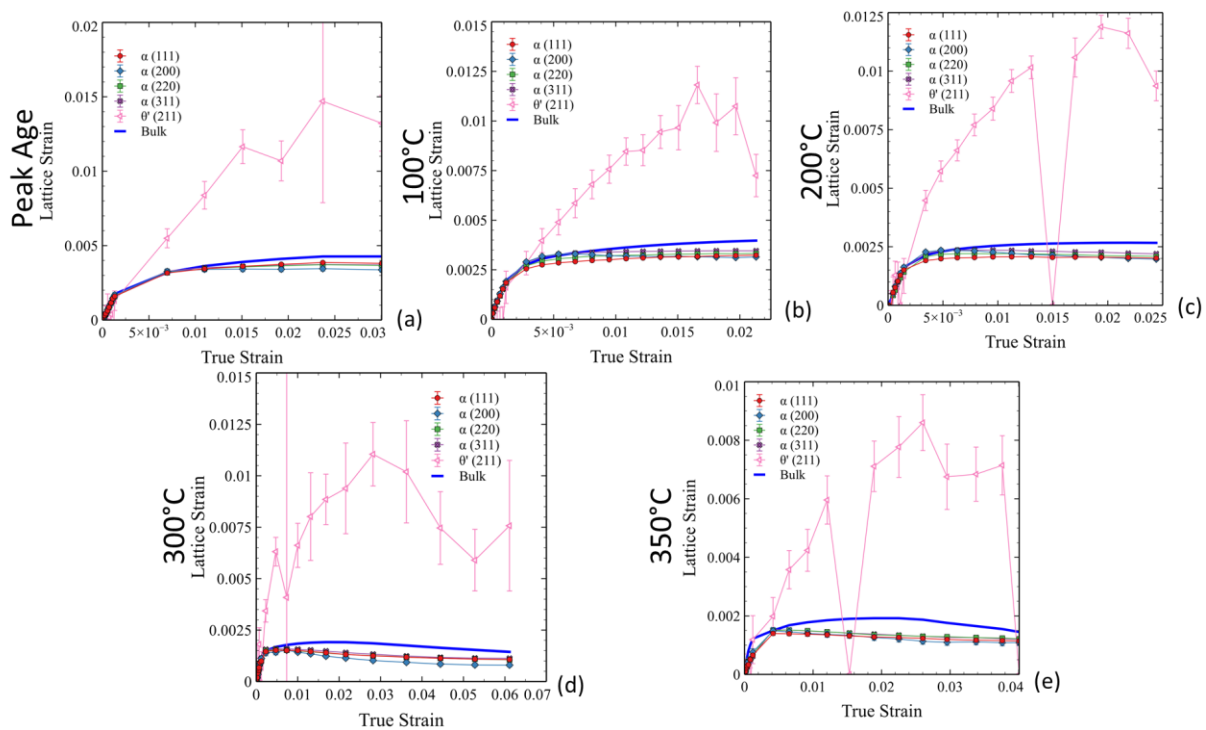

Figure 29.6: Lattice strain evolution in the precipitate and matrix phases in alloy RR350 at a range of temperatures. Note that, in all the elevated temperature experiments, the precipitate lattice strain reaches a maximum and decreases later in the experiment. Zero lattice strain values are indicative of poor peak fit and should be ignored.
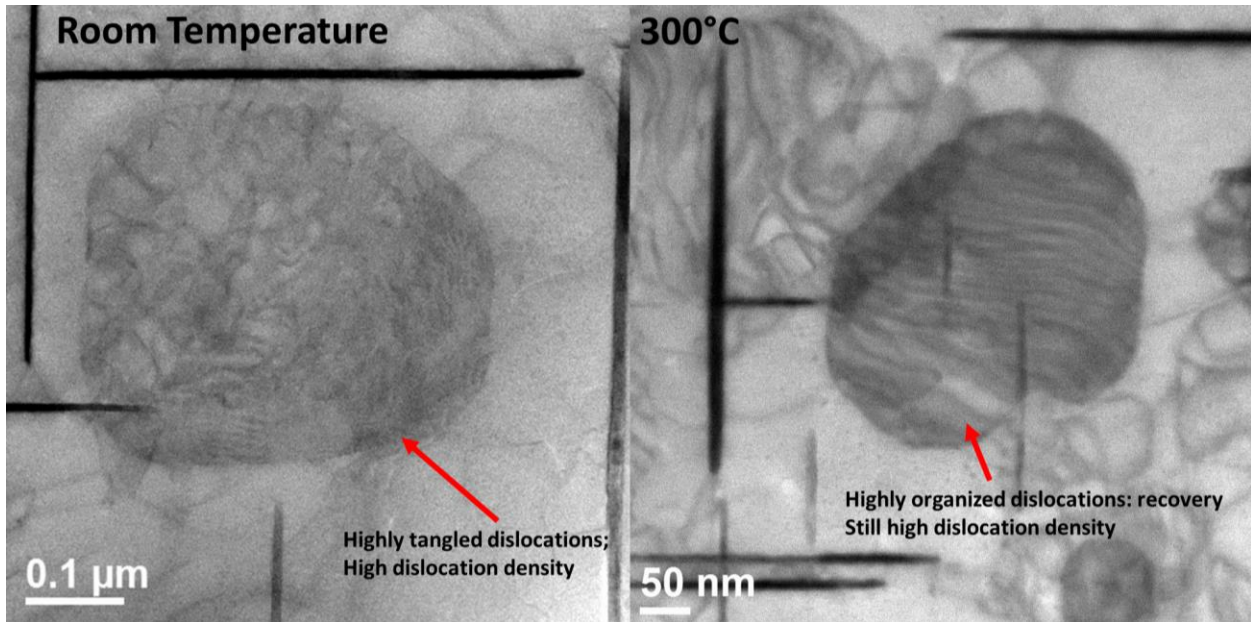
29.7

Figure 29.7: Post-mortem STEM bright field images of alloy RR350. Note the high dislocation density on the interfaces of the in-plane precipitates in both testing temperatures. Also note at room temperature the dislocations are highly disorganized, while at 300°C the dislocations are highly organized.
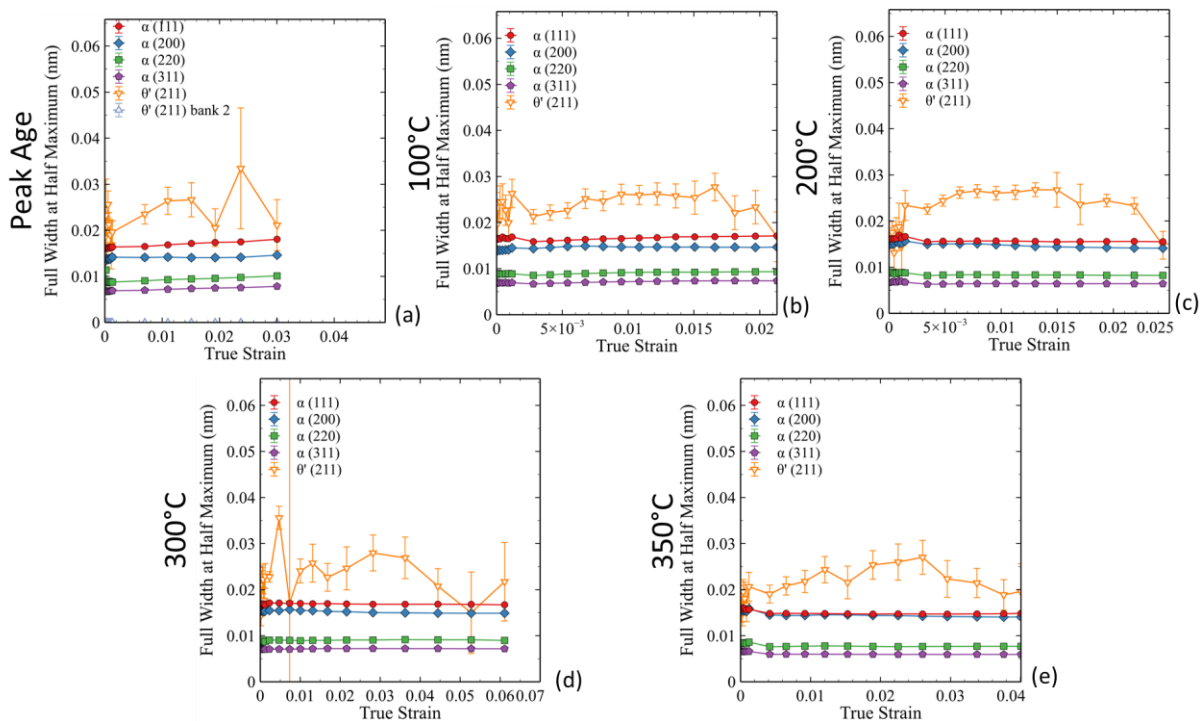

Figure 29.8: Lattice strain versus true strain of the specimen at each temperature condition in alloy RR350. As observed in **Figure 29.6**, there is a downturn in the dislocation peak width at similar strain to that where the downturn in lattice strain occurs for all conditions, apart for room temperature. Also of note is that this downturn occurs at increasing true strain as the temperature increases.

29.8